MIT Libraries | DSpace@MIT

MIT Open Access Articles

Cycloid scanning for wide field optical coherence tomography endomicroscopy and angiography in vivo

Massachusetts Institute of Technology

Cycloid scanning for wide field optical coherence tomography endomicroscopy and angiography *in vivo*

Kaicheng Liang[1,†], **Zhao Wang**[1,†], **Osman O. Ahsen**[1], **Hsiang-Chieh Lee**[1], **Benjamin M. Potsaid**[1,2], **Vijaysekhar Jayaraman**[3], **Alex Cable**[2], **Hiroshi Mashimo**[4,5], **Xingde Li**[6], and **James G. Fujimoto**[1,*]

[1]Department of Electrical Engineering and Computer Science, Research Laboratory of Electronics, Massachusetts Institute of Technology, Cambridge, Massachusetts 02139, USA

[2]Thorlabs, Newton, New Jersey 07860, USA

[3]Praevium Research, Santa Barbara, California 93111, USA

[4]Veterans Affairs Boston Healthcare System, Boston, Massachusetts 02130, USA

[5]Harvard Medical School, Boston, Massachusetts 02115, USA

[6]Department of Biomedical Engineering, Johns Hopkins University, Baltimore, Maryland 21218, USA

Abstract

Devices that perform wide field-of-view (FOV) precision optical scanning are important for endoscopic assessment and diagnosis of luminal organ disease such as in gastroenterology. Optical scanning for *in vivo* endoscopic imaging has traditionally relied on one or more proximal mechanical actuators, limiting scan accuracy and imaging speed. There is a need for rapid and precise two-dimensional (2D) microscanning technologies to enable the translation of benchtop scanning microscopies to *in vivo* endoscopic imaging. We demonstrate a new cycloid scanner in a tethered capsule for ultrahigh speed, side-viewing optical coherence tomography (OCT) endomicroscopy *in vivo*. The cycloid capsule incorporates two scanners: a piezoelectrically actuated resonant fiber scanner to perform a precision, small FOV, fast scan and a micromotor scanner to perform a wide FOV, slow scan. Together these scanners distally scan the beam circumferentially in a 2D cycloid pattern, generating an unwrapped 1 mm × 38 mm strip FOV. Sequential strip volumes can be acquired with proximal pullback to image centimeter-long regions. Using ultrahigh speed 1.3 μm wavelength swept-source OCT at a 1.17 MHz axial scan rate, we imaged the human rectum at 3 volumes/s. Each OCT strip volume had 166×2322 axial scans with 8.5 μm axial and 30 μm transverse resolution. We further demonstrate OCT angiography at 0.5 volumes/s, producing volumetric images of vasculature. In addition to OCT applications, cycloid scanning promises to enable precision 2D optical scanning for other imaging modalities, including fluorescence confocal and nonlinear microscopy.

*Corresponding author: jgfuji@mit.edu.

†These authors contributed equally for this work.

See Supplement 1 for supporting content.

OCIS codes

(170.4500) Optical coherence tomography; (170.3880) Medical and biological imaging; (170.2150) Endoscopic imaging; (170.2680) Gastrointestinal; (170.5810) Scanning microscopy; (120.5800) Scanners

1. INTRODUCTION

Optical imaging catheter devices have had a longstanding clinical impact in the endoscopic imaging of luminal organs such as the gastrointestinal (GI) tract, particularly with optical coherence tomography (OCT) [1–3] and confocal microscopy [4,5]. Side-viewing optical probes, such as for three-dimensional (3D) OCT imaging, were traditionally scanned with rotary and pullback mechanisms at the proximal end [6,7]. Proximal scan actuation was known to result in nonuniform rotational distortion (NURD) and longitudinal distortion [8–10]. Early studies proposed the use of a micromotor to perform rotary scanning at the distal end [11,12], which was recently revisited by multiple groups [13–17]. However, these studies still relied on a proximal motorized actuation for the slow pullback scan, and the micromotor still exhibited NURD [18]. 2D scanning with purely distal mechanisms has been largely limited to forward viewing probes, using microelectromechanical systems (MEMS) [19] or piezoelectric actuators [20–23]. The piezoelectric tubular actuator producing a 2D spiral forward scan has been demonstrated with multispectral imaging [24], OCT [25,26], and nonlinear fluorescence [27–29]. However, the spiral scan inefficiently samples toward the center, results in nonuniform optical exposure, and is known to require frequent trajectory calibration due to amplitude-dependent phase variation of the fiber scanner [20,27]. Lissajous scanning has been proposed [30–32], which also has nonuniform sampling and requires careful control of frequency and cross-coupling between scan axes. Forward viewing piezoelectric probes for OCT and other scanning microscopies have been typically limited to small fields [25] of <3 mm^2.

Tethered capsules as optical probes have been studied for interrogation of the GI wall [33], where more precise spatial control is possible compared to the well-known wireless version [34]. The potential for capsule imaging without sedation, for example, has applications in disease screening. A tethered capsule using a piezoelectric fiber scanner delivering white-light forward imaging was previously reported [35]. This work was followed by an OCT variant [36] and another variant with spectrally encoded confocal microscopy (SECM) [37] for side viewing of the esophageal circumference. Our group developed a micromotor tethered capsule using proximal manual pullback for volumetric and *en face* esophageal OCT imaging of up to 100 cm^2 field-of-view (FOV) in patients, but the manual pullback could not generate rapid volumetric rates [38]. We recently demonstrated what we believe is one of the first distal 2D scanning, circumferential side-viewing scanners incorporated into a tethered capsule, using a micromotor for the rotary (circumferential) scan and a pneumatic scanner for the longitudinal scan [39]. This study suggested the potential for catheter-based 2D scanning side-viewing microscopy *in vivo*, but the pneumatic distal scanner was bulky and difficult to drive rapidly, limiting volumetric rates.

In addition to OCT imaging of microstructure, OCT angiography (OCTA) has also been previously reported for imaging of vasculature without contrast agents [40–44]. Early endoscopic studies used Doppler OCT to visualize relatively large vessels [45,46]. Recently, our group demonstrated ultrahigh speed endoscopic OCTA to visualize 3D microvasculature in the GI tract, using a small diameter micromotor probe [17], a balloon for larger FOV [47], and a piezoelectric scanning probe for forward imaging [48]. The use of distal scanners with high scan stability is critical for endoscopic OCTA.

In this study, we report a new distal 2D precision scanning technology that can achieve rapid volumetric side view imaging with a large FOV using a capsule device. A piezoelectric tube is used to perform a precision fast scan of an optical fiber, and the scanned beam is reflected in the radial direction and rotary scanned around the circumference, generating a cycloid scan trajectory that covers a large circumferential strip. Sequential strip volumes can be acquired using proximal pullback (or push forward) to image centimeter-long regions. We demonstrate 1.17 MHz A-scan rate ultrahigh speed swept source OCT with an imaging area of 1 mm × 38 mm and volume rate of 3 volumes/s, and OCTA at 0.5 volumes/s in the human rectum. The combination of the resonant fiber scanner and micromotor, which are some of the fastest-in-class microscanners available, promises to not only increase frame or volume rates for higher data acquisition rates in OCT, but also to enable precision 2D scanning for other scanning modalities, including fluorescence confocal and nonlinear microscopy.

2. METHODS

A schematic and photograph of the cycloid imaging capsule is given in Fig. 1. A piezoelectric tubular actuator scanned a fiber cantilever at its resonant scan frequency 7030 Hz to produce a 1 mm diameter circle in the focal plane. The circle was then scanned circumferentially by a micromotor at 3 Hz to produce a 1 mm × 38 mm 2D strip FOV in a cycloid scan pattern [49] [Figs. 2(a) and 2(b)], which could be continuously acquired without scanner flyback.

A. Cycloid Scan

The scan geometry is known as a "prolate cycloid," which is part of the larger family of trochoid curves [50]. The scan pattern consists of a circle translated by a length many times the circle diameter to produce a densely sampled strip. As the circular scan is reflected radially by the prism and rotated around the central axis of the motor, the circle is also incrementally rotated about its center [Fig. 2(a)], due to the mirror property of inverting (or "reversing") an image in the axis perpendicular to its surface. Therefore, a fast 1D line scan in this configuration would not generate a raster-like scan or sweep out a strip, but instead generate a translating and rotating line scan. This motivates the need for a 2D circular scan. The mathematical equations defining the cycloid trajectory are derived as

$$\begin{bmatrix} x \\ y \end{bmatrix} = \mathrm{Rot}(\theta) \cdot \begin{bmatrix} r\sin(2\pi f_{\mathrm{fast}}t) \\ r\cos(2\pi f_{\mathrm{fast}}t) \end{bmatrix} + \begin{bmatrix} 0 \\ 2\pi R f_{\mathrm{slow}}t \end{bmatrix}$$

$$= \begin{bmatrix} \cos(2\pi f_{\mathrm{slow}}t + \phi) & -\sin(2\pi f_{\mathrm{slow}}t + \phi) \\ \sin(2\pi f_{\mathrm{slow}}t + \phi) & \cos(2\pi f_{\mathrm{slow}}t + \phi) \end{bmatrix}$$

$$\times \begin{bmatrix} r\sin(2\pi f_{\mathrm{fast}}t) \\ r\cos(2\pi f_{\mathrm{fast}}t) \end{bmatrix} + \begin{bmatrix} 0 \\ 2\pi R f_{\mathrm{slow}}t \end{bmatrix}$$

$$= \begin{bmatrix} r\sin(2\pi(f_{\mathrm{fast}} - f_{\mathrm{slow}})t - \phi) \\ r\cos(2\pi(f_{\mathrm{fast}} - f_{\mathrm{slow}})t - \phi) \end{bmatrix} + \begin{bmatrix} 0 \\ 2\pi R f_{\mathrm{slow}}t \end{bmatrix}.$$

Above, $\mathrm{Rot}(\theta)$ is a rotation matrix, where θ is the instantaneous angle of local rotation that is applied to the circular (fast) scan trajectory, and is a function of the instantaneous angular position of the prism on the micromotor circumferential rotation (slow) axis. The linear term in the slow axis is due to the micromotor scan producing a translation along the circumferential axis. The local rotation has the effect of slowing down (or speeding up) the effective speed of the circular scan, depending on the micromotor direction of rotation. f_{fast} and f_{slow} refer to the resonant frequency of the fast circular scan and the rotational speed of the slow micromotor scan, respectively. r and R are the radii of the circular scan in the focal plane, and capsule, respectively. The angular offset ϕ refers to the initial rotational orientation of the circular scan due to the initial angular position of the circle on the capsule circumference at the start of the scan volume. ϕ is a critical parameter to achieve accurate reconstruction since all other parameters in the equations are pre-determined design constants.

B. OCT System

The OCT system [Fig. 2(c)] was a dual-circulator interferometer and used a 1.3 μm tunable MEMS-VCSEL swept light source [51] running at a 583,490 Hz bidirectional sweep rate, which produced a 1,166,980 Hz A-scan rate. The A-scan rate was tunable and chosen based on the piezoelectric resonant scan frequency 7030 Hz to have an integer (166) number of A-scans per circular scan frame, to facilitate synchronization and reconstruction. The A/D card (ATS 9370, AlazarTech) was optically clocked by a Mach–Zehnder interferometer up to a fringe frequency of 1.1 GHz to achieve an imaging range of 2.0 mm in air. The power incident on the sample from the capsule was 20 mW. The VCSEL sweep bandwidth was 115 nm, and the axial resolution was 12 μm in air (8.5 μm in tissue). The measured system sensitivity was 102 dB using a single reflection from a flat-cleaved fiber in the sample arm, and 98 dB overall after subtracting 4 dB to account for a round trip through the imaging capsule, which had a ~60% one-way (~36% round trip) optical transmission.

C. Capsule Construction

The cycloid scanning capsule was assembled as described here. A quadrupole piezoelectric tube fiber scanning device, which has been previously reported by other groups [20,22], was first constructed. An angle-cleaved optical fiber was mounted to the tip of a 1.5 mm diameter piezoelectric tubular actuator (Boston Piezo-Optics, MA), which was enclosed in a 12 G (2.8 mm diameter) hypodermic tube. The actuator was centered within and electrically

separated from the hypodermic tube housing by a sapphire spacer. The resonant frequency was determined by fiber length and could be mathematically predicted [22] and experimentally verified. The resonance was selected to be about 7 kHz, and measured to be 7030 Hz. A 0.25 pitch gradient index (GRIN) lens (Edmund Optics) was inserted into the tube housing in front of the fiber at a separation that determined the working distance of the optical system. The transverse resolution was designed to be 30 μm FWHM based on simulations (Zemax) with diffraction-limited performance on- and off-axis. Best efforts were made to adhere to the simulated design, including use of GRIN lenses with factory-cut pitches, and optical alignment performed under a magnification stereoscope. The resolution was verified by a knife edge (90–10) power measurement. The focal plane had a slight variation in position around the circumference due to imperfect centration of the micromotor and scanning fiber, and the non-telecentric scan. Aberrations due to the off-axis scan rotated with the circular scan after reflection by the prism, and the plastic outer tube contributed additional aberration, although these were minimal. These effects will be exacerbated in future higher numerical aperture systems, which will likely require custom lens designs. The piezoelectric actuator was soldered to a multiconductor cable (Cooner Wire, CA). The shaft of the 4 mm diameter micromotor (Namiki, Japan) was mounted with a 6 mm diameter brass disc, which increased the moment of inertia for smooth rotation at low speeds. The disc was then mounted with a 2 mm Al-coated prism. The fiber scanner and micromotor were then mounted in 3D-printed holders, which fit snugly and were self-centering within a medical grade polycarbonate plastic machined tube with hemispherical ends.

D. Scanner Control and Data Acquisition

Custom software written in C_{++} controlled the resonant fiber scanner and OCT image acquisition/display. A National Instruments D/A board generated two-channel sinusoidal output with equal and constant amplitude and a phase difference to actuate the fiber scanner and produce a circular scan. The sinusoidal outputs were amplified by a custom voltage amplifier circuit with current limiting capability, to 30 V amplitude a.c., which generated a rapid ~1 mm diameter circular scan in the focal plane. This measurement is below the International Electrotechnical Commission 60601-1 stipulated limit of 42 V amplitude a.c. for medical devices [52]. The micromotor was driven by a driver board (Namiki), generating a slow 38 mm scan around the capsule circumference. The acquisition was synchronized to the resonant fiber trajectory, while the micromotor was externally driven by the driver board, and thus a one-time calibration procedure was required for image reconstruction (Section 2.E, Fig. 3, and Supplement 1). In this study, the resonant frequency was 7030 Hz (166 A-scans per circular scan for ~Nyquist sampling in the fast axis) and the micromotor rotation was 3 Hz (2322 circular scans per volume for ~Nyquist sampling in the slow axis) for structural OCT imaging, and 0.5 Hz (13932 circular scans per volume) for OCTA. The volume was then remapped to a 100×3800 pixel Cartesian grid based on the theoretical scan trajectory equations from Section 2.A above.

E. Image Calibration and Reconstruction

A circular scan of the resonant fiber was generated by applying two phase-separated sinusoidal drive signals to the piezoelectric tube. The phase difference is theoretically 90°, but required a one-time adjustment due to slight asymmetry of the fiber scanner mount and

quadrupole electrodes on the piezoelectric tube. With the micromotor stationary, the phase difference between the sinusoids was empirically tuned until the scan was assessed visually to be sufficiently circular. The only parameter to be determined in the scan trajectory was the phase term ϕ (see Section 2.A above), which described the initial rotational orientation of the circle at the start of each acquisition, and is determined by the starting angular position of the micromotor.

The acquisition was always triggered at the same phase within the period of the sinusoidal drive waveforms (in phase); therefore, the acquisition always started at the same angular position within the circular scan relative to the fiber scanner mount, before reflection by the prism. However, the initial angular position of the micromotor was unsynchronized to the acquisition, which at the start of every acquisition imparted an arbitrary rotational orientation to the circular scan after reflection by the prism. To achieve accurate remapping and reconstruction, a one-time calibration procedure (Fig. 3) was carried out. First, a one-time imaging of a grid pattern was performed, in which a "calibration phase" ϕ_0 was empirically tuned in post-processing until the grid was correctly reconstructed. Thereafter, images acquired at different micromotor angular start positions could be reconstructed by calculating the shift ϕ_1 of the micromotor angular position relative to the calibration image, which could be determined by locating a fiducial (Fig. 4) in the image produced by an internal strut. The fiducial was well-resolved, albeit distorted in the raw unreconstructed image, enabling its use as a marker of the micromotor relative angular position even before reconstruction. The absolute shift $\phi = \phi_0 + \phi_1$ could then be applied to the scan trajectory for reconstruction (Supplement 1).

Raw data volumes were converted to Cartesian coordinates by remapping data points to their theoretical location in time based on the mathematical trajectory. For rapid reconstruction and preview in the acquisition software, we traded off image quality and created lookup tables in MATLAB (MathWorks, MA) based on nearest neighbor interpolation of a Cartesian grid, such that each grid coordinate was mapped directly to a single A-scan in the acquisition. A total of 12 lookup tables were pre-generated using 12 equally spaced values of ϕ from 0 to 2π and used as remapping functions. One of the 12 lookup tables could then be user-selected upon viewing the real-time previews, for an approximate reconstruction using CPU processing in C_{++}. When the volume rate was 3 Hz, the acquisition time per volume was ~0.3 s, and the nearest neighbor reconstruction took ~1.5 s, for a volumetric display rate of ~0.5 volumes/s. Future graphics processing unit (GPU) implementation should improve these speeds. When post-processing for optimal image quality, a more precise ϕ was calculated based on the exact fiducial location, and remapping was performed with cubic spline interpolation for higher quality reconstruction, which took several minutes for each volume in MATLAB. This can also be sped up in the future using GPU-accelerated processing. Larger FOVs were imaged by translating the capsule via the tether, and sequential strip volumes were mosaicked by manual alignment with visual inspection. OCTA was generated by computing OCT signal decorrelation between sequential circular scans (Supplement 1). *En face* images were displayed in square root scale and depth-projected down to 800 μm depth for optimal contrast, although depth-resolved imaging at specific depths was also possible. Cross-sections analogous to traditional B-scans were extracted from reconstructed volumes and displayed in logarithmic scale. Parasitic reflection

artifacts were cropped from cross-sections in regions of low/no signal deep in tissue. Images of living tissue were displayed in sepia for improved contrast. Co-registered OCT/OCTA images were depth projected over 400 μm depth, because deeper image depths had low-signal OCT and generated OCTA that had decorrelation arising from noise rather than blood flow.

F. Clinical Imaging Protocol

The imaging protocol was approved by Institutional Review Board committees at the Massachusetts Institute of Technology (MIT), Veterans Affairs Boston Healthcare System (VABHS), and Harvard Medical School. Written informed consent was obtained prior to imaging. Imaging was performed at the VABHS endoscopy unit. The patient underwent bowel preparation, and was sedated, per colonoscopy protocol. The capsule was introduced by the endoscopist into the patient's anal canal and rectum, before performing a colonoscopy. Capsule positioning was guided by real-time *en face* and cross-sectional OCT imaging. For mosaicking, sequential image volumes were continuously acquired while the operator pulled back or advanced the capsule manually at about 1–2 mm/s, which enabled at least partial overlap of the sequential strip volumes. For structural OCT imaging, the micromotor was set to rotate at 3 Hz. For decorrelation-based OCTA imaging, the micromotor was set to rotate at 0.5 Hz. After OCT imaging was complete, the capsule was withdrawn and the endoscope was introduced for a standard colonoscopy.

3. RESULTS

A. Benchtop Validation

A printed paper grid pattern of 250 μm pitch was imaged to validate the scanning mechanisms and reconstruction algorithm. *En face* OCT imaging of the grid wrapped around the capsule circumference showed good scan accuracy with minimal distortion [Fig. 4(a)]. To demonstrate image mosaicking for a larger FOV, imaging was performed on an alphabetically ordered letter grid rolled into a paper tube, with the capsule pulled back by hand at ~1–2 mm/s through the tube during continuous volumetric acquisition [Fig. 4(b)]. A total of 10 sequential image volumes were acquired over 3.3 s and could be approximately mosaicked to achieve a ~4.5 mm × 38 mm field. The 10 volumes were part of a longer 30-volume acquisition that was used to generate a 10-s video at 3 volumes/s (Visualization 1). The video enables an assessment of volume-to-volume repeatability, as well as overall performance of high volume rate cycloid scanning OCT.

The slow manual longitudinal pullback of the capsule produced a tilt in the letter rows, because the capsule was translated longitudinally during the concurrent rotary scan in the orthogonal direction. The nonuniform speed of the pullback caused the tilts to appear misaligned. Certain letters appeared repeated when the manual pullback was momentarily slower. Loose contact of the paper tube on the capsule allowed the latter to slide, but led to varying contrast along the length of the strips, and contributed in part to an apparent misalignment of the lettering. The micromotor exhibited nonuniform rotational distortion (Supplement 1) that also contributed to the misalignment. Imaging was performed with the capsule gripped in the hand, such that the *en face* plane showed well-resolved fingerprint

contours and palm skin creases [Fig. 4(c)]. Cross-sectional images were also extracted from the reconstructed volume along the slow circumferential axis, which showed depth-resolved imaging into the dermis, similar to traditional OCT B-scans [Fig. 4(d)].

B. Clinical Imaging

Imaging was performed with a patient scheduled for a routine surveillance colonoscopy, during which there were no notable endoscopic findings. OCT structural imaging in the rectum showed regular mucosal patterns indicative of rectal crypt structures in the *en face* plane [Figs. 5(a)–5(c)], while cross-sectional images showed vertical features from crypt architecture and good tissue penetration to about 800 μm depth [Fig. 5(d)]. Imaging at the dentate line showed tissue transition from intestinal crypts of the rectum to relatively smooth squamous epithelium in the anal canal [Figs. 5(e)–5(g)], and the cross-sections showed strong OCT signal from regions of squamous epithelium [Fig. 5(h)]. Large FOV mosaics were generated by manually advancing the capsule into the rectum and continuously acquiring sequential image volumes.

The volumes generated a large FOV with *en face* features approximately mosaicked by manual alignment [Fig. 6(a)]. Each strip of the mosaic showed accurate scanning and undistorted features. Despite the nonuniform speed of the manual longitudinal scan, the partial overlap of each image volume enabled approximate registration and mosaicking based on *en face* features. Co-registered structural and angiographic OCT in the rectum showed regular mucosal patterns and a honeycomb vascular network encircling the crypts [53] [Figs. 6(b)–6(e)]. In the center of the enlargement [Figs. 6(d) and 6(e)], the crypts appear compressed, which could have resulted in slower flow and reduced vascular contrast in that region of the OCT angiogram. The arc-like noise artifacts mimicking the cycloid trajectory were likely due to three factors: (1) synchronization errors between the D/A output and the resonant fiber scanner resulting in small fluctuations in output frequency; (2) the incremental local rotation of the circular scan about its center during the slow micromotor scan; and (3) parasitic tissue motion. These factors produced small frame-to-frame misalignment, which was indiscernible in the structural OCT images, but produced OCTA decorrelation noise.

4. DISCUSSION

To our knowledge, this study is the first demonstration of cycloid scanning for rapid, wide-field endoscopic OCT imaging. The combination of piezoelectric resonant scanning and micromotor scanning enables high precision while also covering a large FOV. The cycloid promises to enable minimally invasive catheter/endoscope imaging not only for high-speed OCT systems, but also for fluorescence confocal and nonlinear microscopy. The study also shows the potential of tethered capsules to image the rectum without endoscopy, extending previous capsule esophageal imaging applications. Approximately 50% of colorectal cancers occur in the rectum and distal colon [54], which suggests that tethered capsules could be a screening tool for a large subset of colorectal cancers.

The cycloid scanner is an important technology to enable distal 2D scanning side-view endomicroscopy. SECM was previously reported for rapid 2D reflectance confocal

microscopy, but has a limited strip width (~200 μm), visualizes a 2D *en face* plane, and is incompatible with scanning microscopies such as fluorescence confocal or nonlinear microscopy [37]. Furthermore, SECM generates a rapid line scan with a swept wavelength source, and therefore cannot be used for volumetric swept-source OCT. The cycloid scanner enables strip imaging at volumetric rates similar to reported capsule SECM frame rates, but with 3D depth-resolved imaging and nearly 9 × larger strip FOV [37]. The cycloid scanner can be extended to finer transverse resolution using a high NA design, as suggested in previously reported capsule designs using a focusing objective rotated by the micromotor [38,39].

The cycloid is simpler to calibrate than the spiral scan, and images can be reconstructed using theoretical equations describing the trajectory. The spiral scan requires amplitude modulation for the slow scan axis and is known to require frequent calibration, as well as complex drive waveforms to rapidly reset the spiral [20]. Moreover, amplitude modulation presents challenges that include transient behavior, phase variation in resonance decay, and mode coupling (cross-coupling) between orthogonal fiber axes. These difficulties can also hinder attempts to perform other 2D scans, such as a linear scan with a rotating axis. In contrast, the cycloid scan requires only a resonant circle at fixed amplitude, which remained repeatable with the same drive parameters over extended periods of several months without recalibration. The micromotor can scan continuously to acquire sequential strip volumes without interruption from flybacks or resets that are needed in other scanning methods.

Commercial catheter/endoscope OCT systems perform real-time, cross-sectional imaging in the rotary side-viewing direction, and volumetric data is acquired by a slow longitudinal pullback at the proximal end of the device. Side-view distal 2D scanning suggests a new paradigm for real-time *en face* OCT imaging that provides rapid volumetric, orthoplane visualization by precision scanning a local region of interest, while also covering a wide circumferential strip. As discussed previously, larger FOVs can be achieved by proximal pullback of the device, mosaicking the circumferential strips to map large regions of luminal organs. The ability to rapidly acquire and view strips of data while also comprehensively imaging a large FOV promises to improve the diagnostic utility of OCT.

The tethered capsule cycloid scanner device has applications in both sedated and unsedated imaging of the gastrointestinal tract. More compact microscanners, such as smaller or flat micromotors and smaller piezoelectric actuators, can be used to reduce the device's rigid length or diameter, which would improve its compactness and broaden its potential clinical applications. Moreover, the cycloid scanner can also be used for small diameter imaging catheters, laparoscopes, or other minimally invasive devices. Smaller diameter cycloid scanners will enable higher NA focusing and faster volume acquisition rates than the large diameter capsules demonstrated in this study.

The cycloid scanner is π times less efficient than a raster scan (Supplement 1), while resonant and micromotor scanners require high data sampling rates. Recent progress in multi-MHz OCT systems [55] using high-speed swept laser technology, fast data acquisition cards, GPUs, and parallel processing is synergistic with rapid scanning. Fluorescence

confocal and nonlinear microscopy can achieve tens of MHz data rates. Cycloid scanners promise to enable a wide range of *in vivo* microscopy applications.

5. CONCLUSION

We demonstrate a new cycloid scanning technology that can be integrated into endoscopic devices for side view, distal 2D precision scanning and wide FOV imaging. Tethered capsule imaging was demonstrated using swept source OCT at a 1.17 MHz axial scan rate with 1 mm × 38 mm fields acquired at 3 volumes/s and larger FOVs achieved by proximal pullback and mosaicking. The current study demonstrates cycloid scanning with a tethered capsule, but this method is also applicable to small diameter catheters, laparoscopes, and other imaging devices. The ability to perform high-speed, precision distal scanning promises to be enabling not only for OCT, but also for fluorescence confocal and nonlinear microscopy.

Supplementary Material

Refer to Web version on PubMed Central for supplementary material.

Acknowledgments

References

1. Tearney GJ, Brezinski ME, Bouma BE, Boppart SA, Pitris C, Southern JF, Fujimoto JG. In vivo endoscopic optical biopsy with optical coherence tomography. Science. 1997; 276:2037–2039. [PubMed: 9197265]

2. Suter MJ, Vakoc BJ, Yachimski PS, Shishkov M, Lauwers GY, Mino-Kenudson M, Bouma BE, Nishioka NS, Tearney GJ. Comprehensive microscopy of the esophagus in human patients with optical frequency domain imaging. Gastrointest Endosc. 2008; 68:745–753. [PubMed: 18926183]

3. Wolfsen HC, Sharma P, Wallace MB, Leggett C, Tearney G, Wang KK. Safety and feasibility of volumetric laser endomicroscopy in patients with Barrett's esophagus (with videos). Gastrointest Endosc. 2015; 82:631–640. [PubMed: 25956472]

4. Kiesslich R, Gossner L, Goetz M, Dahlmann A, Vieth M, Stolte M, Hoffman A, Jung M, Nafe B, Galle PR, Neurath MF. In vivo histology of Barrett's esophagus and associated neoplasia by confocal laser endomicroscopy. Clin Gastroenterol Hepatol. 2006; 4:979–987. [PubMed: 16843068]

5. Canto MI. Endomicroscopy of Barrett's esophagus. Gastroenterol Clin N Am. 2010; 39:759–769.

6. Yun SH, Tearney GJ, Vakoc BJ, Shishkov M, Oh WY, Desjardins AE, Suter MJ, Chan RC, Evans JA, Jang IK, Nishioka NS, Boer JF de, Bouma BE. Comprehensive volumetric optical microscopy in vivo. Nat Med. 2006; 12:1429–1433. [PubMed: 17115049]

7. Adler DC, Chen Y, Huber R, Schmitt J, Connolly J, Fujimoto JG. Three-dimensional endomicroscopy using optical coherence tomography. Nat Photonics. 2007; 1:709–716.

8. van Soest G, Bosch JG, van der Steen AFW. Azimuthal registration of image sequences affected by nonuniform rotation distortion. IEEE Trans Inf Technol Biomed. 2008; 12:348–355. [PubMed: 18693502]

9. Kang W, Wang H, Wang Z, Jenkins MW, Isenberg GA, Chak A, Rollins AM. Motion artifacts associated with in vivo endoscopic OCT images of the esophagus. Opt Express. 2011; 19:20722–20735. [PubMed: 21997082]

10. Uribe-Patarroyo N, Bouma BE. Rotational distortion correction in endoscopic optical coherence tomography based on speckle decorrelation. Opt Lett. 2015; 40:5518–5521. [PubMed: 26625040]

11. Tran PH, Mukai DS, Brenner M, Chen ZP. In vivo endoscopic optical coherence tomography by use of a rotational microelectrome-chanical system probe. Opt Lett. 2004; 29:1236–1238. [PubMed: 15209258]

12. Herz PR, Chen Y, Aguirre AD, Schneider K, Hsiung P, Fujimoto JG, Madden K, Schmitt J, Goodnow J, Petersen C. Micromotor endoscope catheter for in vivo, ultrahigh-resolution optical coherence tomography. Opt Lett. 2004; 29:2261–2263. [PubMed: 15524374]

13. Mavadia J, Xi J, Chen Y, Li X. An all-fiber-optic endoscopy platform for simultaneous OCT and fluorescence imaging. Biomed Opt Express. 2012; 3:2851–2859. [PubMed: 23162723]

14. Li J, de Groot M, Helderman F, Mo J, Daniels JMA, Grünberg K, Sutedja TG, de Boer JF. High speed miniature motorized endoscopic probe for optical frequency domain imaging. Opt Express. 2012; 20:24132–24138. [PubMed: 23187176]

15. Wang T, Wieser W, Springeling G, Beurskens R, Lancee CT, Pfeiffer T, van der Steen AFW, Huber R, Soest GV. Intravascular optical coherence tomography imaging at 3200 frames per second. Opt Lett. 2013; 38:1715–1717. [PubMed: 23938921]

16. Tsai T-H, Potsaid B, Tao YK, Jayaraman V, Jiang J, Heim PJS, Kraus MF, Zhou C, Hornegger J, Mashimo H, Cable AE, Fujimoto JG. Ultrahigh speed endoscopic optical coherence tomography using micromotor imaging catheter and VCSEL technology. Biomed Opt Express. 2013; 4:1119–1132. [PubMed: 23847737]

17. Tsai T-H, Ahsen OO, Lee H-C, Liang K, Figueiredo M, Tao YK, Giacomelli MG, Potsaid BM, Jayaraman V, Huang Q, Cable AE, Fujimoto JG, Mashimo H. Endoscopic optical coherence angiography enables 3-dimensional visualization of subsurface microvasculature. Gastroenterology. 2014; 147:1219–1221. [PubMed: 25172015]

18. Ahsen OO, Lee H-C, Giacomelli MG, Wang Z, Liang K, Tsai T-H, Potsaid B, Mashimo H, Fujimoto JG. Correction of rotational distortion for catheter-based en face OCT and OCT angiography. Opt Lett. 2014; 39:5973–5976. [PubMed: 25361133]

19. Park H-C, Song C, Kang M, Jeong Y, Jeong K-H. Forward imaging OCT endoscopic catheter based on MEMS lens scanning. Opt Lett. 2012; 37:2673–2675. [PubMed: 22743491]

20. Lee CM, Engelbrecht CJ, Soper TD, Helmchen F, Seibel EJ. Scanning fiber endoscopy with highly flexible, 1 mm catheterscopes for wide-field, full-color imaging. J Biophoton. 2010; 3:385–407.

21. Aguirre AD, Sawinski J, Huang SW, Zhou C, Denk W, Fujimoto JG. High speed optical coherence microscopy with autofocus adjustment and a miniaturized endoscopic imaging probe. Opt Express. 2010; 18:4222–4239. [PubMed: 20389435]

22. Liu X, Cobb MJ, Chen Y, Kimmey MB, Li X. Rapid-scanning forward-imaging miniature endoscope for real-time optical coherence tomography. Opt Lett. 2004; 29:1763–1765. [PubMed: 15352362]

23. Rivera DR, Brown CM, Ouzounov DG, Pavlova I, Kobat D, Webb WW, Xu C. Compact and flexible raster scanning multiphoton endoscope capable of imaging unstained tissue. Proc Natl Acad Sci USA. 2011; 108:17598–17603. [PubMed: 22006303]

24. Miller SJ, Lee CM, Joshi BP, Gaustad A, Seibel EJ, Wang TD. Targeted detection of murine colonic dysplasia in vivo with flexible multispectral scanning fiber endoscopy. J Biomed Opt. 2012; 17:021103. [PubMed: 22463021]

25. Huo L, Xi JF, Wu YC, Li XD. Forward-viewing resonant fiber-optic scanning endoscope of appropriate scanning speed for 3D OCT imaging. Opt Express. 2010; 18:14375–14384. [PubMed: 20639922]

26. Lurie KL, Gurjarpadhye AA, Seibel EJ, Ellerbee AK. Rapid scanning catheterscope for expanded forward-view volumetric imaging with optical coherence tomography. Opt Lett. 2015; 40:3165–3168. [PubMed: 26125393]

27. Myaing MT, MacDonald DJ, Li XD. Fiber-optic scanning two-photon fluorescence endoscope. Opt Lett. 2006; 31:1076–1078. [PubMed: 16625908]

28. Xi JF, Chen YP, Zhang YY, Murari K, Li MJ, Li XD. Integrated multimodal endomicroscopy platform for simultaneous en face optical coherence and two-photon fluorescence imaging. Opt Lett. 2012; 37:362–364. [PubMed: 22297353]

29. Liang W, Hall G, Messerschmidt B, Li M, Li X. Nonlinear optical endomicroscopy for label-free functional histology in vivo. Light Sci Appl. 2017; 6:e17082.

30. Moon S, Lee SW, Rubinstein M, Wong BJF, Chen ZP. Semi-resonant operation of a fiber-cantilever piezotube scanner for stable optical coherence tomography endoscope imaging. Opt Express. 2010; 18:21183–21197. [PubMed: 20941015]

31. Liang W, Murari K, Zhang YY, Chen Y, Li XD, Li M-J. Increased illumination uniformity and reduced photodamage offered by the Lissajous scanning in fiber-optic two-photon endomicroscopy. J Biomed Opt. 2012; 17:021108. [PubMed: 22463026]

32. Park H-C, Seo Y-H, Jeong K-H. Lissajous fiber scanning for forward viewing optical endomicroscopy using asymmetric stiffness modulation. Opt Express. 2014; 22:5818–5825. [PubMed: 24663919]

33. Ramirez FC, Akins R, Shaukat M. Screening of Barrett's esophagus with string-capsule endoscopy: a prospective blinded study of 100 consecutive patients using histology as the criterion standard. Gastrointest Endosc. 2008; 68:25–31. [PubMed: 18499107]

34. Iddan G, Meron G, Glukhovsky A, Swain P. Wireless capsule endoscopy. Nature. 2000; 405:417–418.

35. Seibel EJ, Carroll RE, Dominitz JA, Johnston RS, Melville CD, Lee CM, Seitz SM, Kimmey MB. Tethered capsule endoscopy, a low-cost and high-performance alternative technology for the screening of esophageal cancer and Barrett's esophagus. IEEE Trans Biomed Eng. 2008; 55:1032–1042. [PubMed: 18334395]

36. Gora MJ, Sauk JS, Carruth RW, Gallagher KA, Suter MJ, Nishioka NS, Kava LE, Rosenberg M, Bouma BE, Tearney GJ. Tethered capsule endomicroscopy enables less invasive imaging of gastrointestinal tract microstructure. Nat Med. 2013; 19:238–240. [PubMed: 23314056]

37. Tabatabaei N, Kang D, Wu T, Kim M, Carruth RW, Leung J, Sauk JS, Shreffler W, Yuan Q, Katz A, Nishioka NS, Tearney GJ. Tethered confocal endomicroscopy capsule for diagnosis and monitoring of eosinophilic esophagitis. Biomed Opt Express. 2014; 5:197–207.

38. Liang K, Ahsen OO, Lee H-C, Wang Z, Potsaid BM, Figueiredo M, Jayaraman V, Cable AE, Huang Q, Mashimo H, Fujimoto JG. Volumetric mapping of Barrett's esophagus and dysplasia with en face optical coherence tomography tethered capsule. Am J Gastroenterol. 2016; 111:1664–1666. [PubMed: 27808130]

39. Liang K, Traverso G, Lee H-C, Ahsen OO, Wang Z, Potsaid B, Giacomelli M, Jayaraman V, Barman R, Cable A, Mashimo H, Langer R, Fujimoto JG. Ultrahigh speed en face OCT capsule for endoscopic imaging. Biomed Opt Express. 2015; 6:1146–1163. [PubMed: 25909001]

40. Makita S, Hong Y, Yamanari M, Yatagai T, Yasuno Y. Optical coherence angiography. Opt Express. 2006; 14:7821–7840. [PubMed: 19529151]

41. Wang RK, Jacques SL, Ma Z, Hurst S, Hanson SR, Gruber A. Three dimensional optical angiography. Opt Express. 2007; 15:4083–4097. [PubMed: 19532651]

42. Mariampillai A, Standish BA, Moriyama EH, Khurana M, Munce NR, Leung MKK, Jiang J, Cable A, Wilson BC, Vitkin IA, Yang VXD. Speckle variance detection of microvasculature using swept-source optical coherence tomography. Opt Lett. 2008; 33:1530–1532. [PubMed: 18594688]

43. Vakoc BJ, Lanning RM, Tyrrell JA, Padera TP, Bartlett LA, Stylianopoulos T, Munn LL, Tearney GJ, Fukumura D, Jain RK, Bouma BE. Three-dimensional microscopy of the tumor microenvironment in vivo using optical frequency domain imaging. Nat Med. 2009; 15:1219–1223. [PubMed: 19749772]

44. Jonathan E, Enfield J, Leahy MJ. Correlation mapping method for generating microcirculation morphology from optical coherence tomography (OCT) intensity images. J Biophoton. 2011; 4:293–296.

45. Yang VXD, Tang S-J, Gordon ML, Qi B, Gardiner G, Cirocco M, Kortan P, Haber GB, Kandel G, Vitkin IA, Wilson BC, Marcon NE. Endoscopic Doppler optical coherence tomography in the human GI tract: initial experience. Gastrointest Endosc. 2005; 61:879–890. [PubMed: 15933695]

46. Vakoc BJ, Shishko M, Yun SH, Oh WY, Suter MJ, Desjardins AE, Evans JA, Nishioka NS, Tearney GJ, Bouma BE. Comprehensive esophageal microscopy by using optical frequency-domain imaging (with video). Gastrointest Endosc. 2007; 65:898–905. [PubMed: 17383652]

47. Lee H-C, Ahsen OO, Liang K, Wang Z, Cleveland C, Booth L, Potsaid B, Jayaraman V, Cable AE, Mashimo H, Langer R, Traverso G, Fujimoto JG. Circumferential optical coherence tomography angiography imaging of the swine esophagus using a micromotor balloon catheter. Biomed Opt Express. 2016; 7:2927–2942. [PubMed: 27570688]

48. Liang K, Ahsen OO, Wang Z, Lee H-C, Liang W, Potsaid BM, Tsai T-H, Giacomelli MG, Jayaraman V, Mashimo H, Li X, Fujimoto JG. Endoscopic forward-viewing optical coherence tomography and angiography with MHz swept source. Opt Lett. 2017; 42:3193–3196. [PubMed: 28809905]

49. Yong YK, Moheimani SOR, Petersen IR. High-speed cycloid-scan atomic force microscopy. Nanotechnology. 2010; 21:365503. [PubMed: 20705972]

50. Yates, RC. A Handbook on Curves and Their Properties. Edwards, JW., editor. 1947. p. 233-236.

51. Jayaraman, V., Jiang, J., Li, H., Heim, PJS., Cole, GD., Potsaid, B., Fujimoto, JG., Cable, A. Lasers and Electro-Optics (CLEO). IEEE; 2011. OCT imaging up to 760 kHz axial scan rate using single-mode 1310 nm MEMS-tunable VCSELs with >100 nm tuning range; p. 1-2.

52. 60601-1 Medical electrical equipment general requirements for basic safety and essential performance (International Electrotechnical Commission, 2005), pp. 69–70.

53. Wallace M, Lauwers GY, Chen Y, Dekker E, Fockens P, Sharma P, Meining A. Miami classification for probe-based confocal laser endomicroscopy. Endoscopy. 2011; 43:882–891. [PubMed: 21818734]

54. Siegel RL, Miller KD, Fedewa SA, Ahnen DJ, Meester RGS, Barzi A, Jemal A. Colorectal cancer statistics, 2017. CA Cancer J Clin. 2017; 67:177–193. [PubMed: 28248415]

55. Klein T, Huber R. High-speed OCT light sources and systems [Invited]. Biomed Opt Express. 2017; 8:828–859. [PubMed: 28270988]
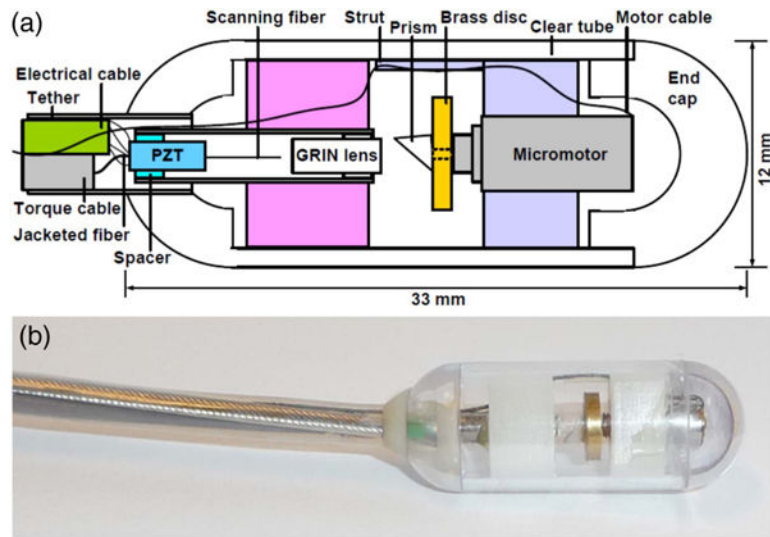
Fig. 1.
(a) Schematic and (b) photograph of cycloid scanning capsule for distal 2D scanning in luminal organs such as the GI tract.
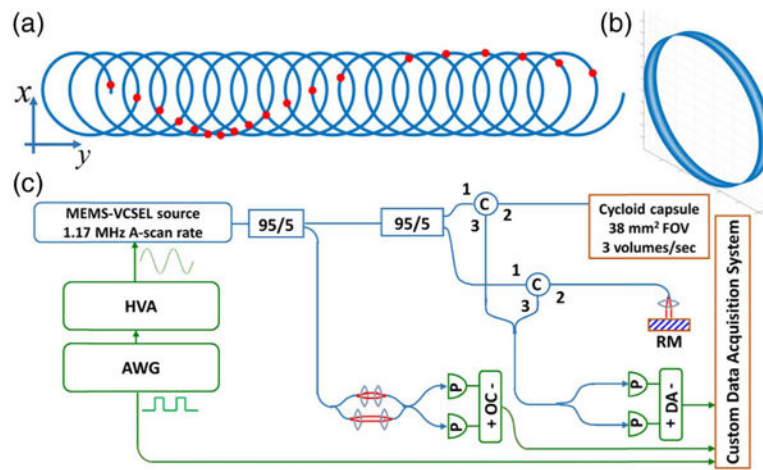
Fig. 2.
(a) Schematic of cycloid scanning geometry when unwrapped on to a flat plane. The red dots indicate spots of each circle scanned at equal temporal frame intervals, showing the slow local rotation of the circle about its center during the scan due to the mirror inversion effect. (b) 3D plot of the cycloid scan in the device geometry. (c) Ultrahigh-speed OCT system. HVA: high-voltage amplifier. AWG: arbitrary waveform generator. C: circulator. RM: reference mirror. P: photodetector. OC: optical clock. DA: differential amplifier.
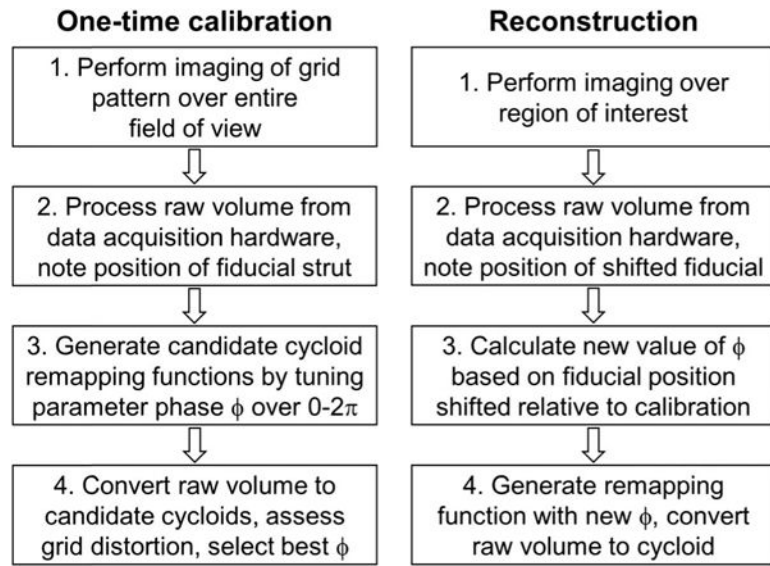
One-time calibration

1. Perform imaging of grid pattern over entire field of view

⇩

2. Process raw volume from data acquisition hardware, note position of fiducial strut

⇩

3. Generate candidate cycloid remapping functions by tuning parameter phase φ over 0-2π

⇩

4. Convert raw volume to candidate cycloids, assess grid distortion, select best φ

Reconstruction

1. Perform imaging over region of interest

⇩

2. Process raw volume from data acquisition hardware, note position of shifted fiducial

⇩

3. Calculate new value of φ based on fiducial position shifted relative to calibration

⇩

4. Generate remapping function with new φ, convert raw volume to cycloid

Fig. 3.
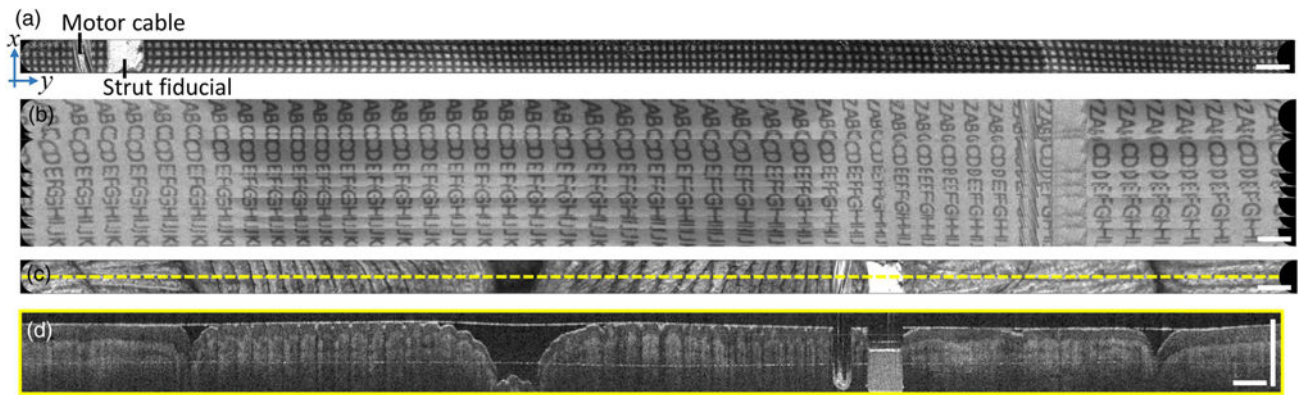Flowchart of one-time calibration and reconstruction procedures for the cycloid scan trajectory.

Fig. 4.
Benchtop imaging. (a) *En face* OCT strip image of printed paper grid. (b) Large field mosaic of 10 sequential strip volumes acquired continuously while manually translating over an alphabetically ordered letter grid. (c) *En face* OCT of human fingers/palm, showing fingerprints and skin creases. (d) Cross-sectional image from center line of volume. *En face* images are mean projections of 800 μm depth. Scale bars are 1 mm.
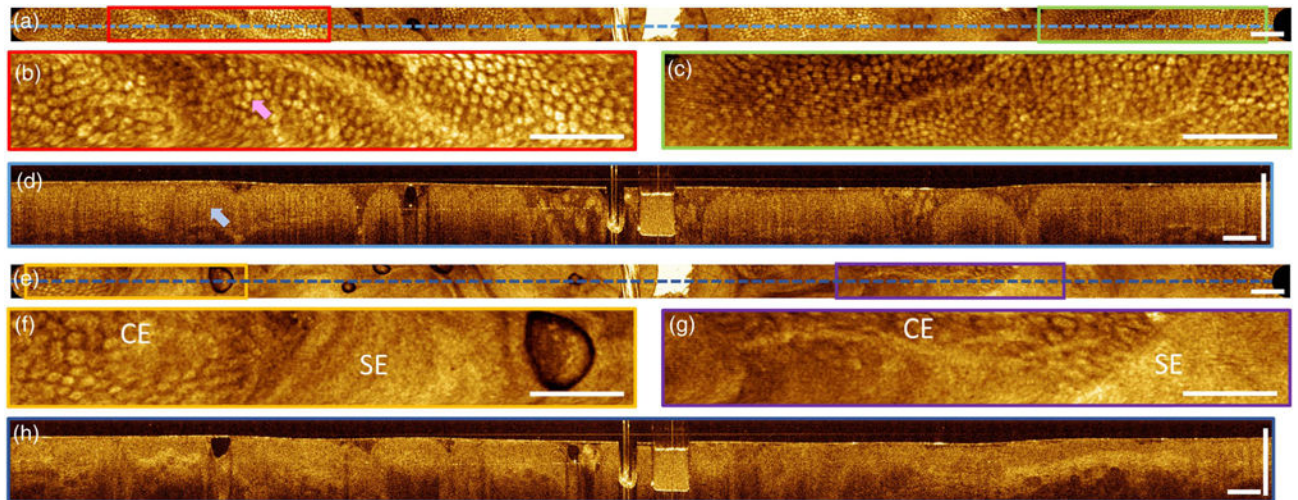
Fig. 5.
Imaging in human subject. (a) *En face* OCT image of human rectum. (b) and (c) Enlargements visualizing crypt structures (pink arrow) of columnar epithelium. (d) Cross section showing vertical crypt architecture (blue arrow). (e) *En face* OCT image of the dentate line (squamo-columnar junction). (f) and (g) Enlargements showing the tissue boundary between columnar epithelium (CE) and squamous epithelium (SE). (h) Cross section showing crypt architecture, and squamous epithelium from the anal canal. *En face* images are mean projections of 800 μm depth. Scale bars are 1 mm.
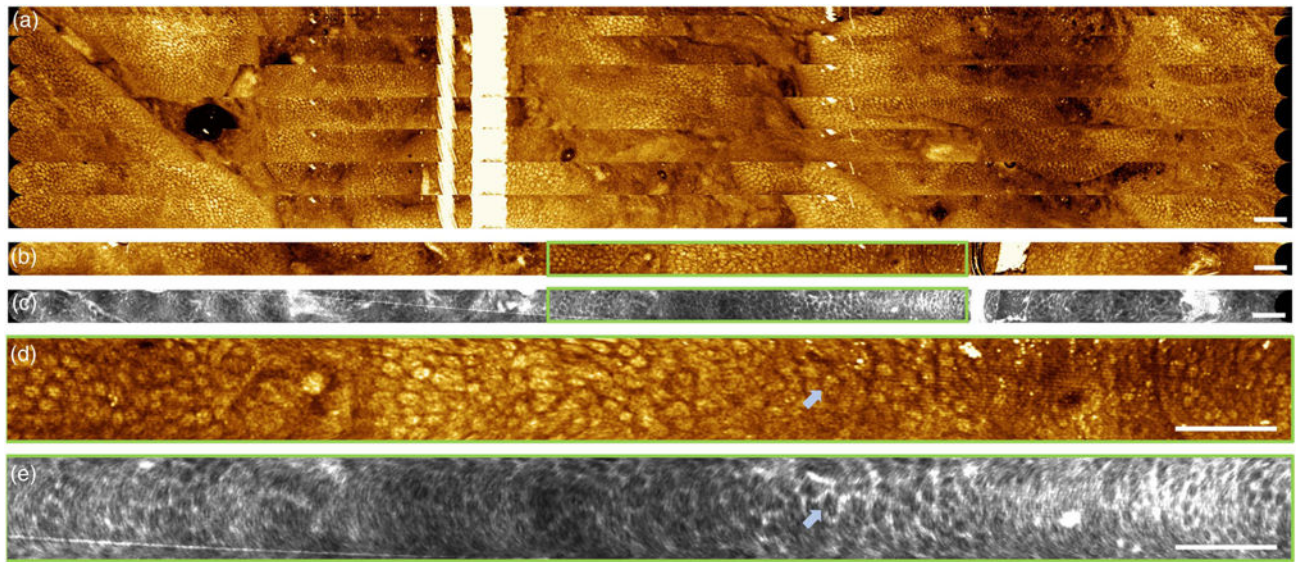
Fig. 6.
(a) Large field mosaic of 10 sequential strip volumes covering a ~7 mm × 38 mm FOV acquired continuously while pushing capsule into rectum at 1–2 mm/s. *En face* images are mean projections of 800 μm depth. (b) and (c) Co-registered OCT and OCTA in rectum. *En face* images are mean projections of 400 μm depth. (d) and (e) Enlargements showing regular mucosal patterns and a honeycomb vascular network encircling the crypts. Arrows point to a crypt encircled by vasculature. Scale bars are 1 mm.